A&A, 699, A343 (2025)
https://doi.org/10.1051/0004-6361/2025
Astronomy & Astrophysics

Nous avons mesuré la forme de 340 000 galaxies pour voir comment elle évoluait à travers les époques

~~DAWN JWST Archive: Morphology from profile fitting of over 340 000 galaxies in major JWST fields~~

~~Morphology evolution with redshift and galaxy type~~

Aurélien Genin[1,2,3,*], Marko Shuntov[1,2,5,*], Gabe Brammer[1,2], Natalie Allen[1,2], Kei Ito[1,4], Georgios Magdis[1,2,4], Jasleen Matharu[1,2], Pascal A. Oesch[1,2,5], Sune Toft[1,2], and Francesco Valentino[1,4]

1 Cosmic Dawn Center (DAWN), Denmark
2 Niels Bohr Institute, University of Copenhagen, Jagtvej 128, 2200 Copenhagen, Denmark
3 Ecole Polytechnique, Institut Polytechnique de Paris, Route de Saclay, 91120 Palaiseau, France
4 DTU Space, Technical University of Denmark, Elektrovej, Building 328, 2800 Kgs. Lyngby, Denmark
5 University of Geneva, 24 rue du Général-Dufour, 1211 Genève 4, Switzerland

Received 13 May 2025 / Accepted 28 May 2025

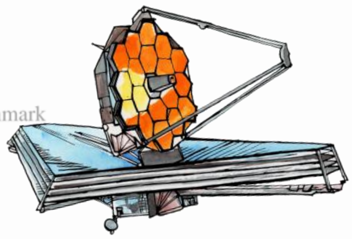

RESUME

ABSTRACT

En utilisant des images publiques du télescope spatial James Webb (JWST), nous avons observé 340 000 galaxies très très loin dans l'Univers afin de mesurer leur forme. Notre but est de comprendre pourquoi et comment certaines galaxies arrêtent de produire de nouvelles étoiles.
Nous avons confirmé que les galaxies s'éteignent (les scientifiques parlent de "quenching") quand elles deviennent plus compactes. Nous avons aussi montré que le centre des galaxies mourantes semble grossir plus vite que leur périphérie.
Tout ce travail vient s'ajouter à une large base de données sur les galaxies dans l'Univers primitif observées par le JWST et utiles aux astrophyisicien.nes.

Key words. techniques: image processing – catalogs – galaxies: evolution – galaxies: structure

QUEL INTERET ?

En observant le ciel, nous savons que les galaxies existent sous différentes formes.

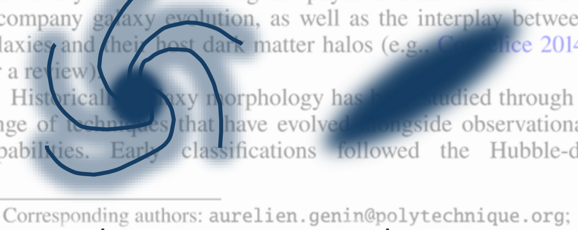

De précédents astrophysiciens ont inventé des moyens de mesurer ces différences de formes à l'aide de nombres. L'objectif est de voir plus précisément comment la forme des galaxies évolue avec le temps.

Un nombre très souvent utilisé est l'indice de Sérsic. Il est petit (environ 1) pour les galaxies spirales, et plus grand (4 et plus) pour les galaxies elliptiques.

* Corresponding authors: aurelien.genin@polytechnique.org; marko.s...dk

studies of galaxy structure, revealing, for instance, that the size distribution at fixed luminosity follows a log-normal form at $z \lesssim 0.3$ (Shen et al. 2003). The Galaxy Zoo project leveraged SDSS imaging to produce visual classifications for hundreds of thousands of galaxies (Lintott et al. 2008), enabling studies of morphological diversity and its connection to environment and star formation (e.g., Schawinski et al. 2014). At intermediate redshifts, the *Hubble* Space Telescope (HST) played a transformative role through legacy programs such as GEMS (Rix et al. 2004), COSMOS (Koekemoer et al. 2007), and CANDELS (Grogin et al. 2011; Koekemoer et al. 2011), which enabled hig[illegible] out to $z \sim 3$. These datasets allowed for extensive morphological analyses, [illegible] are more co[illegible] galax-ies at fixed mass (e.g., Daddi et al. 2005; Trujillo et al. 2007; Bar[illegible] they undergo size growth primarily via dry mergers (e.g., van der Wel [illegible] et al. 2017). However, the mechanisms that drive galaxy quenching remain debated, for example, whether morphological transformation and the cessation of star formation are causally linked, or whether they occur independently as consequences of other processes (e.g., Tacchella et al. 2015). Disentangling this connection requires large, statistically robust samples of galaxies with reliable morphological measurements spanning a wide redshift rang[illegible] time. Furthermore, at higher redshifts ($z \gtrsim 3$), HST imaging becomes limited t[illegible] tly traces young stellar populations and can bias morphological interpretations ([illegible]). Nevertheless, these surveys laid the groundwork for the construction of large morphological catalogs (e.g., York et al. 2000; van der Wel et al. 2012; Kawinwanichakij et al. 20[illegible] d structural transformation of galaxies over more than 10 billion years of cosmic history.

Pour observer les galaxies et leur évolution dans le temps, les télescopes doivent sonder très loin dans l'Univers (rappelons que plus on observe loin, plus on remonte dans le temps).

C'est ce qu'ont fait de nombreux télescopes, comme Hubble et maintenant le JWST. Cela permet de disposer d'un très grand nombre d'observations, le JWST allant même plus loin que Hubble !

The James Webb Space Telescope (JWST) has opened a new era in the study of galaxy morphology, enabling rest-frame optical measurements out to $z \gtrsim 7$ with unprecedented depth and resolution. Studies based on JWST observations have revealed the evolution of galaxy morphology and size for both star-forming and quiescent galaxies out to unprecedented redshifts (e.g., Varadaraj et al. 2024; Ormerod et al. 2024; Allen et al. 20[illegible]24; Yang et al. 2025). These studies show that quiescent galaxies rema[illegible] aller effective radii and higher Sérsic indices, even at early times. Nevertheless, most JWST morphological analyses to date have focu[illegible] color-selected subsamples, or have been limited to individual fields. A[illegible] ical catalog across different major JWST fields and redshifts. This limits [illegible] studies of gal[illegible] as quiescent galaxies at the full depth and breadth enabled by JWST.

Les astronomes ont des régions préférées du ciel qu'iels observent avec différents télescopes. Cela permet de comparer leurs mesures et de mieux comprendre l'Univers. Celles que nous avons utilisées sont appelées : EGS, GOODS, COSMOS, UDS (Sondage Ultra Profond !).

In this work, we build one of the largest and most uniform morphological catalogs to date using JWST imaging, enabling consistent structural measurements across multiple fields and redshifts. We utilize publicly available mosaics from the DAWN JWST Archive (DJA, Valentino et al. 2023), which compiles deep NIRCam imaging from major extragalactic surveys, including CEERS, PRIMER (UDS and COSMOS), and GOODS. These are accompanied by matched photometric redshifts and physical parameters. To measure galaxy morphology, we carry out two-dimensional surface brightness profile fitting using SourceXtractor++ (Bertin et al. 2020; Kümmel et al. 2020), a modern, scalable tool optimized for catalog-level model fitting in large multiband datasets. We fit each galaxy with both a single-component Sérsic profile (Sérsic 1963) and a two-component Bulge+Disk (B+D) model consisting of an exponential disk ($n_S = 1$) and a de Vaucouleurs bulge ($n_S = 4$). This dual-model approach allows us to probe structural diversity more flexibly and to derive key parameters, such as the Sérsic index (n_S), the effective radius, the axis ratio, and the bulge-to-total ratio (B/T). We apply this modeling to all sources above a flux an[illegible] pho-logical catalog spanning approximately 340 000 sources across $0 <$ [illegible] commu-nity to carry out detailed statistical studies of galaxy morphology evolution throughout cosmic time.

[illegible] function (PSF) reconstruction are presented in Section 2. In Section 3, we des[illegible] ring the morphology and sizes of galaxies across such a large field. In Section 4, we present our results on the correlation between morphology and the UVJ diagram, as well as the size evolution in the Sérsic and B+D models. We summarize our results in Section 5. We adopt a Planck Collaboration VI (2020) ΛCDM cosmology with $H_0 = 67.4\,\mathrm{km\,s^{-1}\,Mpc^{-1}}$, $\Omega_{\mathrm{m},0} = 0.315$. All magnitudes are expressed in the AB system (Oke 1974).

Nous avons entrepris de mesurer la forme de BEAUCOUP PLUS de galaxies en observant toutes ces grandes régions profondes du ciel en même temps.

QUELLES DONNEES UTILISONS-NOUS ?

This work uses NIRCam images (Rieke et al. 2005) from public surveys of the JWST, processed as part of the DAWN JWS[illegible] online reposit[illegible] gs, and spectr[illegible] described in m[illegible] 5). In this work, we carry out morphological measurements in several m[illegible] al area of ~500 arcmin^2. We focus on the following fields:

1. EGS from CEERS (DD-ERS 1345 Finkelstein et al. 2023);
2. GOODS from JADES (GTO 1180, 1181, 1210, 1287 Eisenstein et al. 2023);
3. UDS from PRIMER UDS (GO 1837 Donnan et al. 2024);
4. COSMOS from PRIMER COSMOS (GO 1837 Donnan et al. 2024).

Comme nous utilisons des images publiques, prises par d'autres astronomes utilisant le JWST, il est toujours bon de les mentionner.

Table 1 presents the area and photometric bands used in these fields and their 5σ depths (computed from empty apertures by Weibel et al. 2024).

2.1. Images

The images used in this work are drawn from the DJA [illegible] the wh[illegible] 2 gds-grizli-v7.2, gdn-grizli-v7.3, primer-uds-north-g[illegible] r-cosmos-west-grizli-v7.0, and primer-cosmos-east-grizli-v7.0.

The DJA [illegible] ges, in photometric units (10 nJy), which we used to run SourceXtractor++, alongside [illegible] provide the inverse variance distribution. For source detection, we used the inverse-variance weighted stack of the long-wavelength filters (specified with `ir` in place of the filter in the image name). We did not

Les images ont déjà été traitées par le Cosmic DAWN Center (où j'ai effectué mon stage qui m'a amené à faire ce travail) afin d'être prêtes à être utilisées par les scientifiques.

Table 1. Summary of the fields covered in this work.

Field	Area (arcmin^2)	Depth (mag)	Bands
EGS	82.0	29.16	F115W, F150W, F182M, F200W, F210M, F277W, F356W, F410M, F444W
GOODS	67.3	29.93	F090W, F115W, F150W, F200W, F277W, F356W, F444W
PRIMER-UDS	224.4	28.51	F090W, F115W, F150W, F200W, F277W, F356W, F444W
PRIMER-COSMOS	127.1	28.62	F090W, F115W, F150W, F200W, F277W, F356W, F444W

Notes. All images are from the DJA and were processed prior to this work. The survey areas and 5σ depths computed from empty apertures correspond to the F277W band and were calculated by Weibel et al. (2024).

apply any PSF convolution, since SourceXtractor++ convolves the source models with the corresponding filter PSF (see Sect. 2.3).

2.2. Catalogs

The DJA also provides photometric and photo-z catalogs produced with SExtractor (Bertin & Arnouts 1996) and EAZY (Bram[illegible] catalogs as our principal list [illegible] sources for each field. Although we perfo[illegible] TOR++ (Sect. 3.1), we cross-matched with the DJA sources to ensure model [illegible]. This ap[illegible] physical parameters from spectral energy distribution (SED) fittings w[illegible] ork, we used the EAZY output to investigate morphology evolution as a function of [illegible].

Nous avons également utilisé les mesures effectuées par les astrophysicien.nes de DAWN sur d'autres propriétés de ces galaxies : leur distance, leur masse, leur couleur, leur luminosité...

2.3. Point spread function reconstruction

Accurate model fitting requires precise characterization of the instrument's PSF. The PSF results from light diffraction at the aperture of the telescope and defines the resolution limit of JWST. We empirically modeled the PSF from the final mosaics using PSFEx (Bertin 2011), which builds a model for the PSF by fitting a set of basis functions to point sources provided in an in[illegible] PSFEx accurately models the NIRCam PSF on mosaics.

To select point sources, we developed a method inspired by [illegible] MAG_AUTO measurements from SExtractor. The parameter MU_MA[illegible] pixel of a source, while MAG_AUTO denotes the Kron-like elliptical aperture magnitude. In the MU_MAX/MAG_AUTO plane (shown in Fig. 1), the poi[illegible] slope equal to one (referred to in this paper as the "starline"), and extended sources form a distinctive cloud above it. We added thresholds for MAG_AUTO: a minimal value to avoid selecting saturated

Tout télescope (tout comme l'appareil photo de votre téléphone) prend des photos toujours un peu floues. Nous devons mesurer ce flou pour le corriger lorsque nous mesurerons la forme des galaxies.

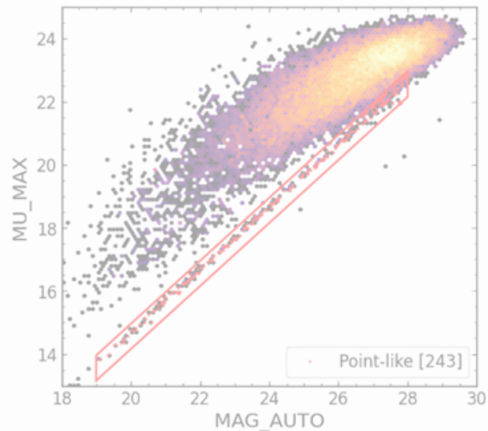

Fig. 1. Point-like sources selection for PSF estimation. The plot shows the distribution (log scale) of sources from the GOODS-S field (F200W) in the MU_MAX/MAG_AUTO plane. The red box shows the starline selection of point-like sources, with the starline indicated by red dots.

Pour ce faire, on observe des étoiles (dans la Voie lactée, notre galaxie) et la forme avec laquelle elles apparaissent. Avec le JWST, elles ressemblent à cela !

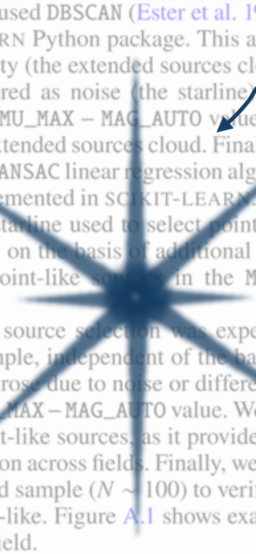

sources [illegible] al value to avoid including sources in the extended sources cloud.

[illegible] gression. However, to avoid bias from the extended sources cloud, we first applied [illegible] this point cloud and remove it. We used DBSCAN (Ester et al. 1996), implemented in the SCIKIT-LEARN Python package. This algorithm identifies cores of high density (the extended sources cloud) while excluding points considered as noise (the starline). We then applied a threshold on the MU_MAX – MAG_AUTO value to further remove outliers from the extended sources cloud. Finally, we detected the starline using the RANSAC linear regression algorithm (Fischler & Bolles 1981), implemented in SCIKIT-LEARN. The threshold and width around the starline used to select point-like sources were chosen empirically on the basis of additional tests. Fig. 1 shows the selection of point-like sources in the MU_MAX/MAG_AUTO plane.

The point-like source selection was expected to physically yield the same sample, independent of the band used. However, slight differences arose due to noise or differences in the threshold used for the MU_MAX – MAG_AUTO value. We chose the F200W band to select point-like sources, as it provided the most consistent starline detection across fields. Finally, we visually inspected a randomly selected sample ($N\sim100$) to verify that the selected sources were point-like. Figure A.1 shows examples of the PSFs in the GOODS-S field.

3. Morphological measurements

NOS MESURES

3.1. SourceXtractor++

In[illegible] galaxy morphologies measured from JWST images. To accomplish this, we used SourceXtractor++ (hereafter abbreviated as SE++; Bertin et al. 2020; Kümmel et al. 2020), the successor of the classic SExtractor Bertin & Arnouts (1996), which performs bri[illegible] and images. The principal advantage of SE++ is that it is optimized [illegible] – it can simult[illegible] ics and

Nous ne sommes pas partis de zéro. Nous avons utilisé un outil appelé SourceXtractor++ (le successeur de SEXtractor, oui c'est son vrai nom) qui peut mesurer la forme des galaxies avec un modèle donné (comme l'indice Sérsic).

in different bands, without the need for prior sample selection, cutout creation, and masking. Additionally, its flexible model fitting allows the user to define any model using a simple Python configuration file. In the following, we describe our models and catal...

Dans notre travail, nous avons utilisé deux modèles de forme pour les galaxies.

3.2. Brightness profile models

To measure galaxy morphology, we modeled the brightness profile ... full control over the model. To maximize scientific applications, we ...

Le premier est le modèle Sérsic. Il considère les galaxies comme des taches de lumière et mesure leur forme en fonction de la netteté de leurs bords.

1. The Sérsic model (Sérsic 1963), parameterized by a single shape parameter, the Sérsic index n_S; the effective radius R_e; ... flux f_{tot}. In this work, we fit for the two components of the ellipticity, e_1 and e_2, ...ked to (a/b) and θ. The priors used for these parameters are presented in Fig. B.1.
2. The Bulge + Disk (B+D) model, a composite of an exponential disk (... 1) and a de Vaucouleurs bulge (... Sérsic ... parametrized ... effective radii ... disk, ... and bulge, R_{bulge}; the ... ratios $(a/b)_D$ ... $(a/b)_B$; a common angle θ_{BD}; the total flux of both components, $f_{BD,tot}$; and the bulge-to-total ratio $B/T = f_{B,tot}/f_{BD,tot}$. The B/T prior is a bell curve ranging from 5×10^{-5} to 1, with a mean and spread that increase as a function of wavelength.

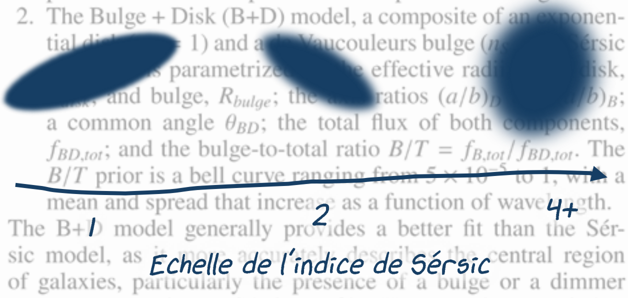

The B+D model generally provides a better fit than the Sérsic model, as it more accurately describes the central region of galaxies, particularly the presence of a bulge or a dimmer center compared to a Sérsic profile. However, because it has more parameters, it is more computationally intensive and can, in some cases, lead to degeneracy in the model parameters, especially for ... not be distinguishable.

Le second modèle est appelé Bulbe+Disque. Il s'agit de la superposition de deux modèles de Sérsic :

- Un d'indice 4 pour le centre (le bulbe) de la galaxie
- Un d'indice 1 pour la périphérie (le disque) de la galaxie.

The SE++ tool performs model fitting simultaneously on multiple i... this work, we constrain the morphological parameters (R_{eff}, n_S, (a/b), and θ) to be identical across all bands for a given source. This approach yields final values that represent a weighted average over the entire wavelength range used (0.9–5 μm). The SE++ configuration file def... available on GitHub[1].

3.3. Tiling

It is theoretically possible to run SOURCEXTRACTOR++ directly on the full mosaics from the DJA. However, because of speed and computing power limitations, we chose to tile the full images. ... We divided the mosaics into 2′ × 2′ tiles, with 0.5′ overlap, ...

Ce modèle B+D décrit mieux certaines galaxies qui ont un noyau très brillant (à cause d'un trou noir supermassif par exemple).

3.3.1. Catalog merging

To merge the sub-catalogs, we iterated over each tile to append them and create a catalog covering the whole field. At each iteration step, we cross-matched with the previously appended sub-catalogs and discarded the matched duplicates from the overlap regions. For sources that are matched (in the overlap region), we chose the one with the smallest uncertainty in the F200W magnitude, as measured by SOURCEXTRACTOR++. As the model fitting was performed independently for the Sérsic and B+D models, this step was performed separately to produce one catalog per model. The F200W band was chosen because it has better resolution compared to the LW channel, and galaxies are generally brighter in it than in other bands of the SW channel.

Finally, we cross-matched the two model-fitting catalogs with the DJA catalogs. This step allowed us to remove false detections (which were frequent near the edges of images), retain the same list of sources, and provide additional morphological measurements to the DJA catalogs. We chose a threshold of 0.3″ as the cutting distance to validate a match. This threshold was set manually using the histogram of angular distances produced by the cross-match. This value corresponded to 5 pixels in the LW channel and 10 pixels in the SW channel of NIRCam, which was acceptable and could be the result of differences between the source centroids estimated in SEXTRACTOR and SOURCEXTRACTOR++.

3.3.2. Merging of the model and residual images

The SE++ tool produces model and residual images. We merged only the model sub-images and generated a mosaic residual image afterward. To merge the sub-images, we used the `reproject_and_coadd` function from the `reproject` Python package (Robitaille 2018), which reprojected and co-added the images on a frame specified by the World Coordinate System (WCS) of the native DJA images. This ensured that the merged full model images had the same pixel scale, center, and orientation as the DJA images. We used this to generate mosaic residual images by subtracting the mosaic model images from the source DJA images.

3.4. Flagging and completeness

As mentioned previously, our aim was to add morphological measurements to the DJA catalogs. Therefore, by cross-matching, we retained the same number of rows (sources) in our catalogs as in the DJA catalogs. Furthermore, we added a `flag` keyword with four possible values as follows:

- **0** : the source was not fitted (no morphological data).
- **1** : a potential artifact occurred during model fitting.
- **2** : fitting was performed successfully. This value gives science-ready data.
- **3** : the source has S/N < 3 or a magnitude fainter than the 5σ depth of its corresponding survey. The S/N was computed by SOURCEXTRACTOR++ on the detection image.

The distribution of the `flag` values is shown in Fig. 2. Seventy to eighty percent of the sources were successfully fitted (`flag=2`). This indicates that the SOURCEXTRACTOR++ minimization algorithm converged and the parameter values were not ...

Pour exécuter SourceXtractor++ sur toutes nos images, nous devons les découper en petites tuiles. Il s'agit simplement de ne pas trop faire mal aux ordinateurs qui devront effectuer les mesures.

... some parameters remaining at their initial values or that strayed to the ... this indicates a poor fit; therefore, we flagged such sources. For the Sérsic model, this includes sources with $(a/b) > 0.99$, $|n_S - 0.36| < 10^{-4}$, $n_S > 8.35$, or $n_S < 0.301$. For the B+D model, this includes $(a/b)_D > 0.9999$, $(a/b)_D < 0.10001$, or $|(a/b)_D - 0.5| < 10^{-5}$. These values were chosen manually by identifying artifacts in the parameter distribution and by visual

[1] https://github.com/AstroAure/DJA-SEpp/blob/main/config/sepp-config.py

Table 2. Completeness of the morphology measurements using SourceXtractor++.

Field	DJA	Sérsic	Bulge+Disk	Both
CEERS	67 035	52 604 (78.5%)	59 046 (88.1%)	**51 329 (76.6%)**
GOODS-S	57 355	44 931 (78.3%)	52 754 (92.0%)	**44 016 (76.7%)**
GOODS-N	65 481	53 291 (81.4%)	58 852 (89.9%)	**51 465 (78.6%)**
PRIMER-UDS (N)	68 857	58 947 (85.6%)	67 134 (97.5%)	**57 945 (84.2%)**
PRIMER-UDS (S)	65 864	57 397 (87.1%)	64 537 (98.0%)	**56 476 (85.7%)**
PRIMER-COSMOS (E)	50 655	42 359 (83.6%)	48 496 (95.7%)	**41 597 (82.1%)**
PRIMER-COSMOS (W)	51 362	40 493 (78.8%)	46 964 (91.4%)	~~**39 704 (77.3%)**~~
Total	426 609	350 022 (82.0%)	397 783 (93.2%)	**342 892 (80.4%)**

Notes. Values in the table show only sources with F277W magnitudes below the 5σ depth of each field, and a S/N >3. For the SourceXtractor++ columns, the values correspond to sources successfully fitted (flag=2); see Sect. 3.4. The percentages are relative to the DJA catalogs with the same magnitude and S/N cut.

Toutes les galaxies qui ont été correctement mesurées : 340 000 galaxies !

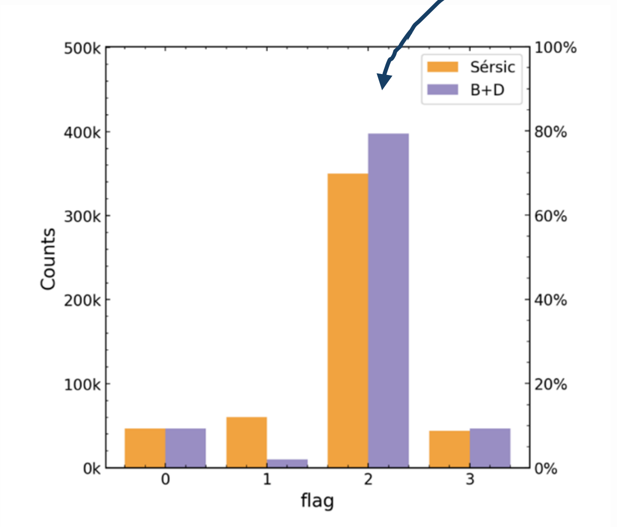

Fig. 2. Histogram of the flag values for the full catalogs. The percentages are relative to the total number of sources in the DJA catalogs. Two distinctive histograms for the Sérsic and Bulge+Disk models are shown bec[...] major-ity (70–80%) of sources are correctly fitted and provides science-ready morphol[...]

Pour des raisons mystérieuses, le programme échoue parfois à mesurer la forme d'une galaxie. Nous identifions ces échecs et marquons celles qui ont été correctement mesurées. Ainsi, nous savons que nous avons pu mesurer la forme de 80 % des galaxies présentes sur les images !

inspection. These sources should be handled with care by the user.

Since the list of detected and measured sources by SourceXtractor++ is slightly different from the initial DJA li[...] ta-logs. Table 2 presents the number of galaxies in each field used in t[...] 2) in each model (Sérsic and B+D) from our work.

The completeness was measured relative to the number of galaxies [...] cut on S/N and magnitude as S/N >3 and mag <5σ depth (flag=3) on both. In total, our catalog consists of 342 892 sources with reliable model fitting and science-ready, making it one of the largest morphological catalogs based on JWST observations.

A total of 80.4% of the DJA S/N >3 and mag <5σ depth sources were successfully fitted with both a Sérsic and a B+D model. The completeness is higher for the B+D model than for the Sérsic model. This is likely because the B+D model is a better description for some sources whose Sérsic model parameters tend toward the minimum or maximum allowed values (therefore classified as flag=1). Finally, we analyzed the distribution of certain physical parameters (F277W magnitude, z_{phot}, mass, and Kron radius) for the non-detected sources (flag=0) and potential artifacts (flag=1). We did not find any significant correlation between these parameters, indicating that the incompleteness due to flag=1 is not biased with magnitude, redshift or stellar mass.

Therefore, we consider our morphological catalogs to have a relatively high completeness compared to the DJA, and, as such, they provide highly valuable information for studying the morphology of galaxies and its evolution through cosmic time, as demonstrated in Sect. 4.

3.5. Comparisons with previous work

To validate our measurements, we compared them with previous morphological catalogs in the same fields, particularly van der Wel et al. (2012). These catalogs contain Sérsic modeling performed using *Hubble* Space Telescope (HST) observations in the same fields used in this work: GOODS, EGS, UDS, COSMOS. By cross-matching them with our catalog and selecting only early-type galaxies (see Eq. (2)), we find 3263 matches with S/N >10.

The size and morphology of galaxies are known to differ in different wavelength ranges. To ensure that we compared morphologies measured at similar observer-frame wavelengths, we used the measurements in F160W from van der Wel et al. (2012). However, since our measurements correspond to the averaged morphology over NIRCam's wavelength range (~1–5 µm), we scaled the effective radii R_{eff} in van der Wel et al. (2012) to 2.5 µm using the following scaling relation:

Pour nous assurer de la fiabilité de nos mesures, nous comparons certaines d'entre elles avec des études antérieures qui ont utilisé des outils différents.

$$\frac{\Delta \log R_{\mathrm{eff}}}{\Delta \log \lambda} [\ldots] \quad (1)$$

which [...] be the wav[...] We note that a more complex version of this relation has been proposed by the same a[...] of redshift and stellar mass. However, we adopted this simpler and more general relation for comparison purposes.

Figure 3 shows the one-to-one comparisons between the two works for R_{eff} (top middle panel) and the Sérsic index n_{S} (top

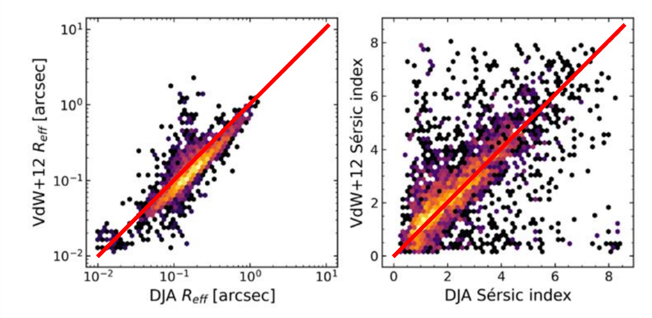

Fig. 3. Comparison between Sérsic model fitting in our work and van d... compares effective radii $R_{\rm eff}$ and Sérsic index n. We corrected the $R_{\rm eff}$ val... 2.5 µm using Eq. (1), in order to match the average wavelen... of our JWS... each cell in log scale. Gray dotted lines show identical values between the two... right panel), as well as the histograms of $R_{\rm eff}$, n_S, and the axis ratio (a/b) (bottom panels). In general there is good agreement in the ... from our measurements. One reason for the slight offset could be the scaling ... ling, the trend inverses and our effective radii are smaller than those of van der Wel et al. (2012).

Idéalement, tous les points devraient se trouver sur la diagonale rouge. Mais comme nous avons utilisé des images et des outils différents, il est normal qu'il y ait une certaine dispersion. Cependant, ils suivent à peu près la bonne tendance. **Nos mesures sont donc bonnes !**

4. Morphological evolution with redshift and galaxy type

QUE POUVONS-NOUS APPRENDRE ?

To demonstrate the scientific application of our morphological catalogs, we investigated statistical distributions of several morphology indicators as a function of redshift and galaxy type. Our measurements cover a wide range of redshifts, enabling studies ... we used the photo-z, rest-frame colors, and other physical parameters from the DJA EAZY catalogs. In particular, we investigated morphological evolution as a function ... vs. star-forming).

La principale motivation de ce travail était d'étudier la différence de forme entre les galaxies qui forment de nouvelles étoiles et les galaxies "mortes" (appelées galaxies quiescentes).

Pour distinguer les galaxies qui forment des étoiles des galaxies mortes, on peut regarder leur couleur. Les jeunes étoiles sont généralement bleues car elles sont plus chaudes, tandis que les vieilles étoiles sont rouges car elles sont plus froides. (Oui, c'est l'inverse des couleurs de votre robinet...)

... and redshift, we used the UVJ color diagram to select star-forming ... ple, the UVJ selection criteria for quiescent galaxies ... with redshift (Williams et al. 2009). However, for our qualitative analysis, we adopted a redshift-independent selection corresponding to the $0.7 < z < 1.3$ range used in Schreiber et al. (2016), who also investigated the morphology dependence of the UVJ diagram from HST observations:

C'est pourquoi nous savons que les galaxies mortes sont plus rouges que les galaxies en formation d'étoiles. Nous pouvons donc regarder la forme des galaxies et la comparer à leur couleur !

$$UVJ_{\rm quiescent} = \begin{cases} V - J < 1.6, \text{ and} \\ U - V > 0.88(V - J) + 0.49. \end{cases} \quad (2)$$

In addition, we focused our analysis on $\log M_\star/{\rm M}_\odot > 10$, `flag=2`, and S/N >10, resulting in 13 685 galaxies. This ensured that our sample had sufficiently high S/N and robust morphological estimates from the model fitting.

First, we investigate the location of galaxies in the UVJ diagram as a function of the Sérsic index, n_S, and redshift. Fig. 4 shows the UVJ diagram in six redshift bins at $0 < z < 6$ (in different panels), color coded by the Sérsic index. The dotted lines mark the regions separating star-forming and quiescent galaxies (Eq. (2)). Fig. 4 shows a clear correlation between the Sérsic index and UVJ colors. There is a gradient of the Sérsic index, n_S, in a direction roughly orthogonal to the boundary between quiescent and star-forming galaxies, such that galaxies with a higher Sérsic index preferentially populate the redder and quiescent UVJ region. This trend holds for the different redshift bins. For $z > 4$, the samples are too small to draw statistically robust conclusions, especially for quiescent galaxies.

Second, because we also used B+D models to fit the galaxies in our catalogs, we could analyze how their B/T values populate the UVJ diagram. For this analysis, we used the B/T measured in the F200W band because it offers better resolution, being in the SW channel. Figure 5 shows UVJ diagrams for three broad redshift ranges and three B/T ranges. The color indicates the B/T value, with the color scale indicated at the top. We also show the contours estimated by kernel density. Fig. 5 shows that bulge-dominated galaxies ($B/T > 0.6$) preferentially occupy the quiescent region, whereas disk-dominated galaxies ($B/T < 0.2$) occupy the star-forming region. Intermediate galaxies that show both bulges and disks ($0.2 < B/T < 0.6$) form a diverse population that can be classified as both star-forming and quiescent based on their UVJ colors. However, there is a trend showing that galaxies with a higher B/T preferentially occupy the quiescent UVJ region. At $z > 3$ there are more galaxies with higher B/T that are star-forming than quiescent. This results from the relative rarity of quiescent galaxies at these epochs, as well as from the presence of a population of compact star-forming galaxies (e.g., blue nuggets, Barro et al. 2013; Dekel & Burkert 2014, which we discuss further in the next part of this section). These qualitative trends from the independently fitted B+D model are in good agreement with those from the ... the morphological measurements.

To further investigate the correlation between bulge- and disk-... morphology and star formation activity, we defined two classes based on the two independent morphology estimates, n_S and B/T, as follows:

1. Bulge-dominated galaxies: $n_S > 1$ and $B/T > 0.5$.
2. Disk-dominated galaxies: $n_S < 4$ and $B/T < 0.5$.

... of whether a galaxy is disk- or bulge-dominated and explore how ...

In Fig. 6, we show the UVJ diagrams in the same redshift ranges as in Fig. 4, with color indicating the ... different classes: red for bulge-dominated galaxies and blue for disk-dominated galaxies. We plotted kernel density contour lines for each class. This classification is consistent with the broad conclusion that quiescent galaxies are bulge-dominated and star-forming galaxies are disk-dominated.

The disk-dominated sample still exhibits a degree of bimodality, with a small population of quiescent galaxies. ... is typically associated with disk galaxies, quiescent disks do exist. At lower masses, quenching is often environmentally driven, particularly via strangulation (Larson et al. 1980; Moran et al. 2007), ram pressure stripping (Gunn & Gott 1972), and galaxy harassment (Moore et al. 1996, 1998) in dense environments (Peng et al. 2010; Cortese et al. 2021). At higher masses, some fast-rotating quiescent disks can

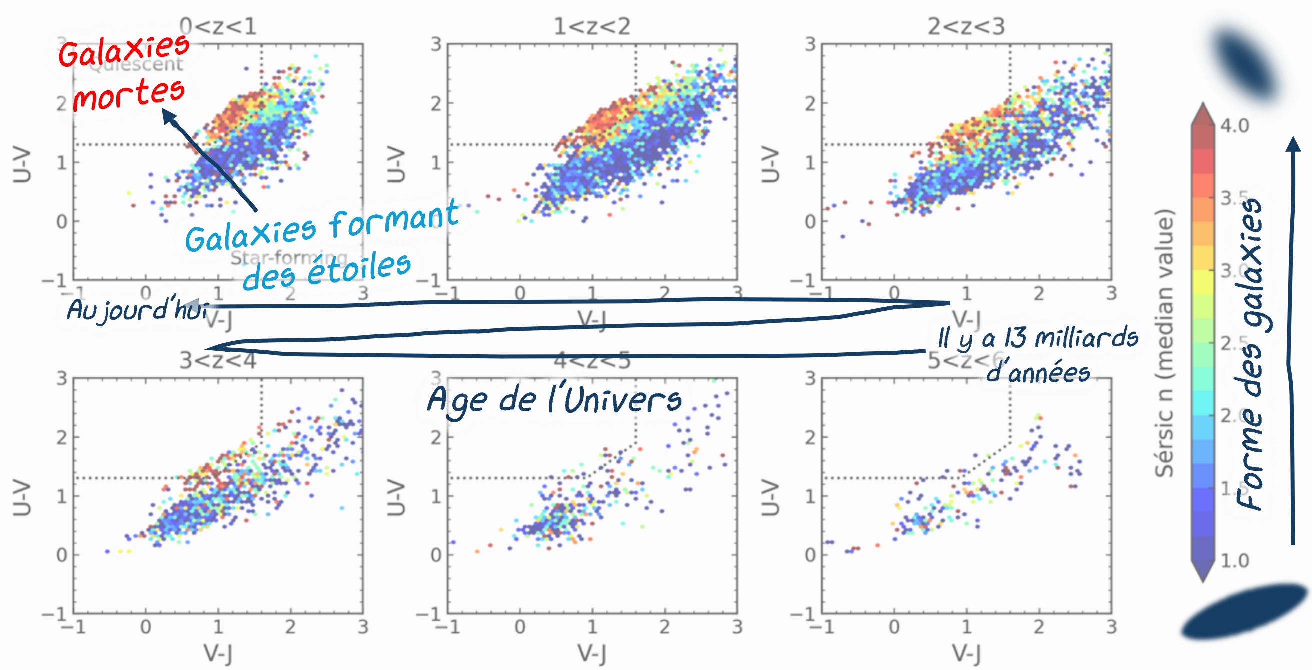

Fig. 4. Distribution of Sérsic indices, n_S, in the UVJ color space for different redshift ranges, for galaxies with $\log M_\star/M_\odot > 10$. The color of each hexagonal bin represents the median value of n_S, as indicated by the colorbar. The dotted line shows the quiescent vs. star-forming separation using Eq. (2). The quiescent region is predominantly populated by galaxies with high Sérsic indices ($n_S \gtrsim 3$).

form through a combination of mild dissipative contraction and secular evolution (Toft et al. 2017; D'Eugenio et al. 2024). These quiescent disks may also result from gas exhaustion following a compaction event or mergers that preserve disk kinematics but sup... 2015).

Bulge-... cent UVJ region out to $z \sim 3$, with a small bimodality appe... in the star-forming region at higher redshifts. This indicates that bulges can still be actively forming stars, especially at earlier cosmic times, but by $z < 1$, most have migrated toward quiescence. Thi... bulge growth coincides with or precedes quenching, consistent with theoretical and observational evidence for compaction-driven quenching (e.g., Barro et al. 2013, 2014; Tac... 2015, 2016). The location of bulge-dominated galaxies in the UVJ dia... dominated population ... supports a fast quenching scenario in which lower mass, young, star-forming galaxies undergo rapid quenching ($t_Q < 2$ Gyr e.g., Moutard et al. 2018; Belli et al. 2019). This is consistent with the blue nugget phase, where galaxies experie... quenching into red nuggets (e.g., Dekel & Burkert 2014; Zolotov et al. 2015; Barro et al. 2017). ... the lower ... bulge-domin... tent with the inverted Hubble classification evolution ... form as disks and evolve to bulges (e.g., Quilley & de La... 2022).

This qualitative analysis of the correlation between quenching and morphology is consistent with the current picture from both theory and observations. Importantly, by providing morphological measurements from JWST for such a large sample, our work paves the way for more in-depth and quantitative population studies that can unveil the details of galaxy quenching and the accompanying morphological transformations.

... redshift ... for galaxies classified by their morphology type (namely, bulge- and disk-dominated). We analyzed the radii from the two independent models: the effective radius r_e from the Sérsic model, and the disk effective radius r_{disk} and bulge effective radius r_{bulge} ... verting the measured angular radii using the z_{phot} given in the DJA EAZY catalogs.

... 7, we show the size evolution with z_{phot} for the Sérsic effective, disk, and bulge size measures for galaxies with ... of $\approx 4 \times 10^{10}\,M_\odot$. We show the trend for all galaxies, disk- and bulge-dominated as defined in Sect. 4.1. We note that our sizes were computed as the average size over the ~1–5 μm range, whereas size-redshift evolution studies typically use the size measured in ... optical range over the studied redshift range. This means that our measurements probe the rest-frame ... at $z < 0.5$; however, this approach ... introduce differences when comparing our results with studies that base their size measurements on a single band for a ... redshift range.

Our measurements show that the overall size (r_e, from the Sérsic model) of all galaxies with $\log M_\star/M_\odot > 10$ increases with redshift from about 1 kpc at $z \sim 5$ to ~2.5 kpc at $z \sim 0.5$. Disk-dominated galaxies show larger sizes by about 0.1–0.2 kpc compared to the whole sample, and increase with time, while

La figure ci-dessus montre comment la forme des galaxies est liée à leur couleur (et donc au fait qu'elles produisent ou non de nouvelles étoiles).

Nous constatons que les galaxies mortes ont toujours un indice de Sérsic élevé, alors que les galaxies en formation d'étoiles ont un indice de Sérsic faible.

Cela confirme que les galaxies en formation sont généralement des galaxies à disque et que les galaxies mortes sont elliptiques.

De plus, nous constatons que cette conclusion reste vraie à différentes époques (bien qu'il y ait moins de galaxies mortes dans l'Univers primitif parce qu'elles n'ont pas encore eu le temps de s'éteindre).

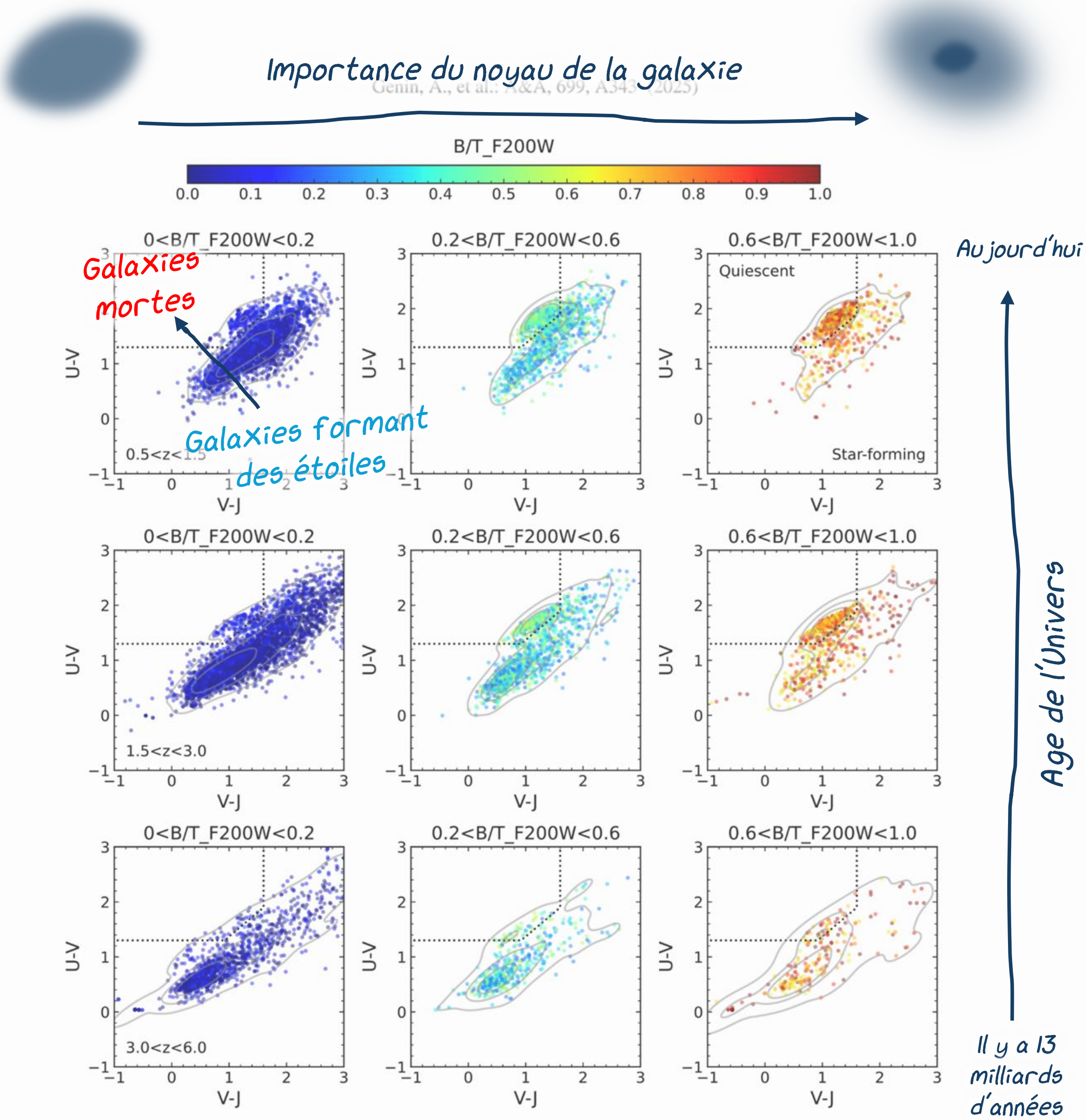

Utiliser le modèle Bulbe+Disque donne des résultats similaires :
Les galaxies mortes ont généralement un noyau brillant et un disque sombre.
Les galaxies en formation d'étoiles ont généralement un noyau sombre et un disque brillant.

Mais l'inverse est également vrai :
Les galaxies dont le noyau est brillant sont généralement mortes.
Les galaxies dont le disque est brillant sont généralement en train de former des étoiles.

Et nous ne savons pas encore si l'un provoque l'autre (est-ce la mort de la galaxie qui la rend plus dense ? Ou est-ce sa compactification qui la fait mourir ?) ou s'il y a un effet externe qui provoque les deux.

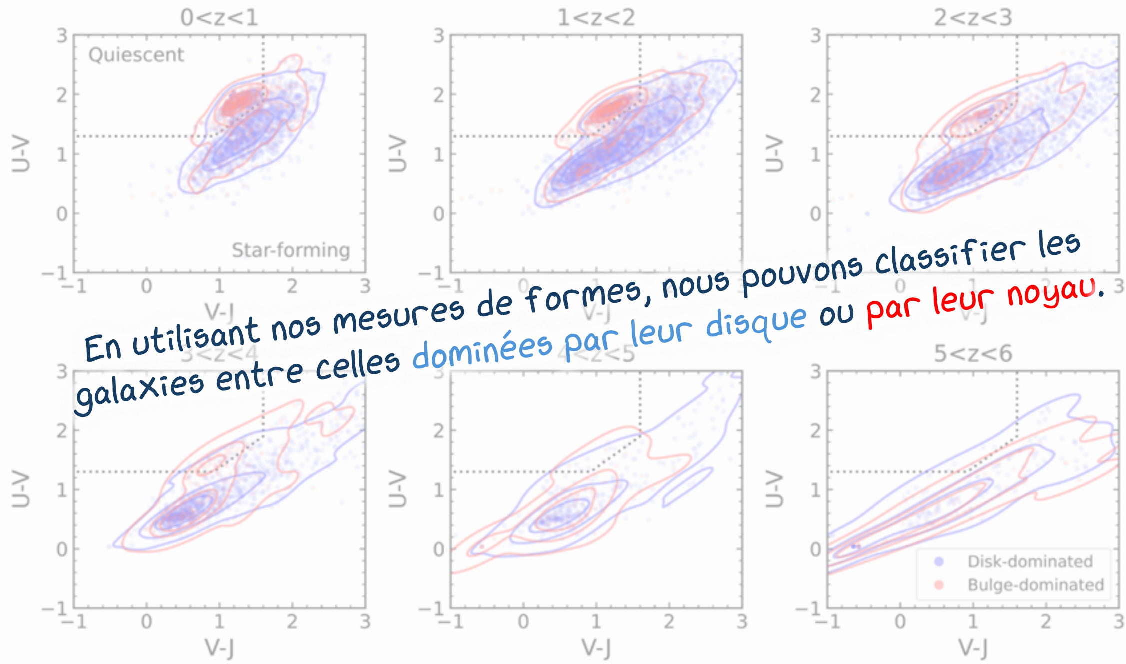

En utilisant nos mesures de formes, nous pouvons classifier les galaxies entre celles dominées par leur disque ou par leur noyau.

Les galaxies grandissent avec le temps, mais les galaxies mortes ont connu une augmentation soudaine de leur taille, alors que les galaxies en formation d'étoiles ont connu une croissance régulière.

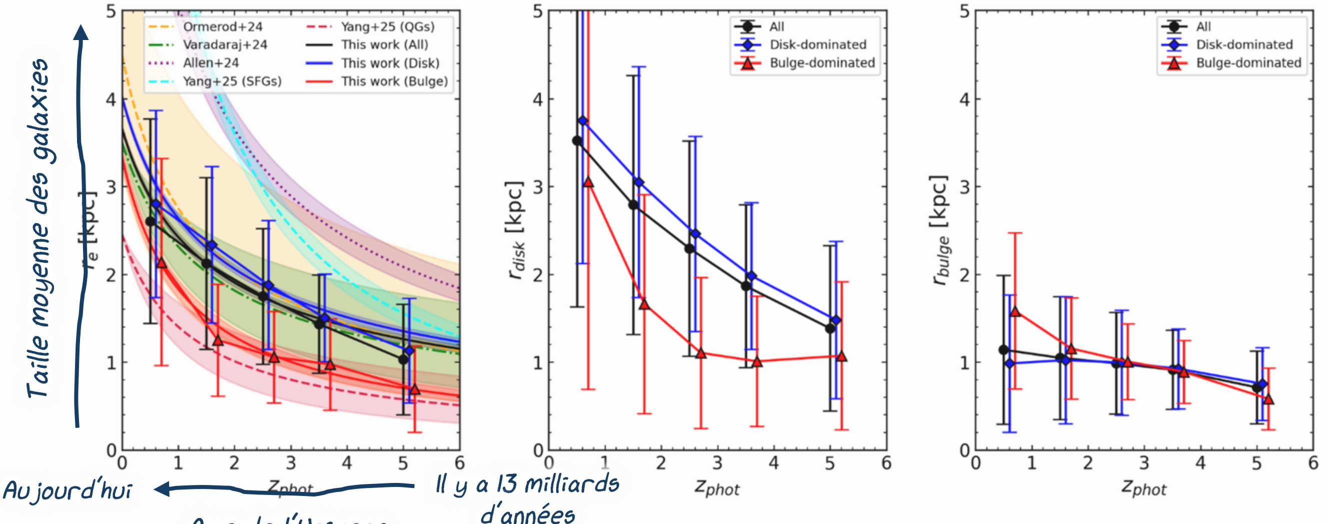

Fig. 7. Evolution of galaxy sizes as a function of redshift. The plots show the Sérsic effective radius r_e (left), the disk effective radius r_{disk} (center), and the bulge effective radius r_{bulge} (right) as a function of z_{phot} for $\log M_\star/M_\odot > 10$ galaxies. This corresponds to a mean mass of $\approx 4 \times 10^{10}$ $M_\odot$. ... et al. (2024), Allen et al. (2025) and Yang et al. (2025).

Nous avons également mesuré la taille des galaxies. Comme nos images contiennent des galaxies datant d'époques cosmiques très différentes, nous sommes en mesure de suivre l'évolution de leur taille en fonction de l'âge de l'Univers.

disk-dominated population exhibiting larger disks by approxi- ... population exhibiting bulge sizes of about 1 kpc. However, the ...

Les galaxies sont aujourd'hui 2 à 3 fois plus grandes qu'au début de l'Univers !

Nous le savions déjà, mais grâce à nos mesures de forme, nous pouvons distinguer l'évolution des galaxies en formation d'étoiles de celle des galaxies mortes.

Nous avons découvert que les galaxies mortes ont grandi plus tard, mais plus rapidement, que les galaxies en formation d'étoiles !

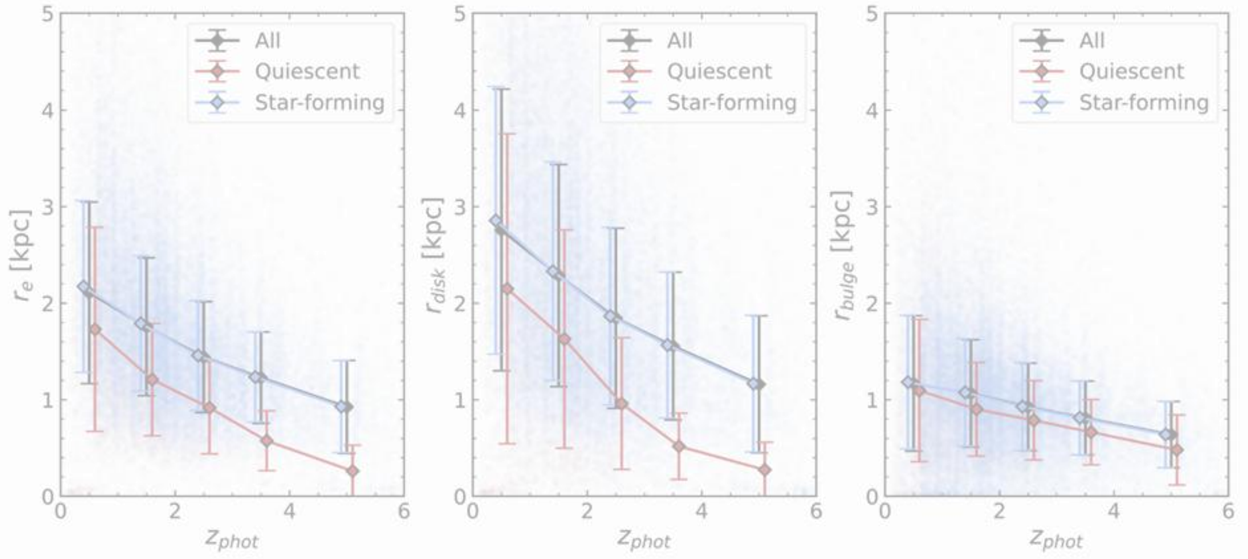

Fig. 8. Evolution of the sizes of quiescent and star forming galaxies with $\log M_\star/M_\odot > 10$. The plots show the Sérsic effective radius r_e, the disk effective radius r_{disk}, and the bulge effective radius r_{bulge} as a function of z_{phot}. Galaxies are classified as quiescent or star-forming based on their UVJ colors. The points and error bars indicate the mean and 1 σ dispersion in the corresponding z_{phot} bin.

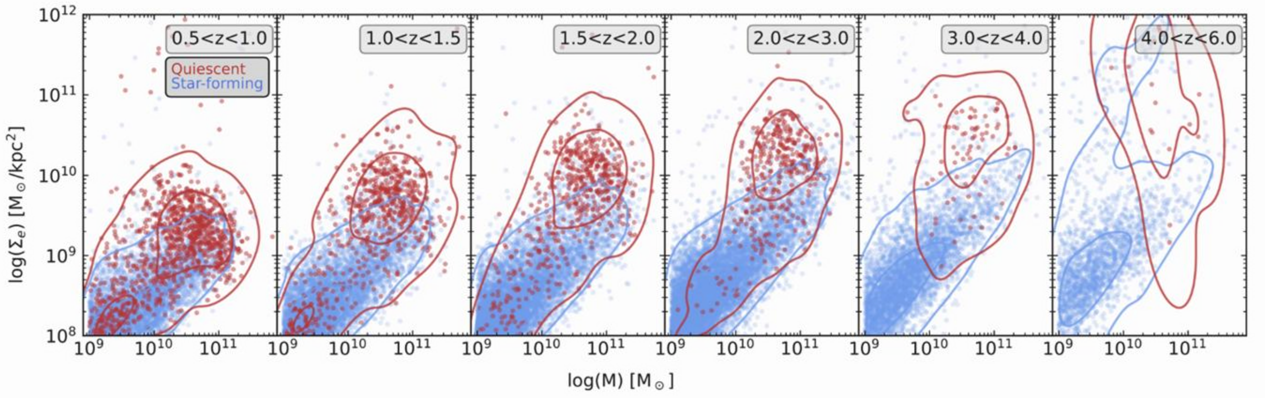

Fig. 9. Evolution of the stellar mass surface density, Σ_e. Shown are masses and redshifts from the DJA, calculated using EAZY, and effective radii, r_e, measured by SOURCEXTRACTOR++ in this work. Galaxies are classified as quiescent or star-forming according to their position in the UVJ diagram. The ... galaxies such that $\log M_\star/M_\odot > 9$.

En combinant la forme, la taille et la masse, nous avons calculé la "densité" des galaxies.

Ce qui est très intéressant, c'est que les galaxies mortes dans l'Univers primitif étaient ~10 fois plus denses qu'aujourd'hui !

Overall, as expected, quiescent galaxies have smaller sizes than star-forming ... with redshift, from ~0.2 kpc for the earliest quiescent galaxies at $z \sim 5$ to ~2 ... and increase in size from ~1.2 kpc to ~2.6 kpc by $z \sim 0.5$. This shows that the size growth of quiescent galaxies is steeper than that of star-forming galaxies. This size evolution is consistent with previous studies showing that both populations experience growth over time, driven by minor mergers and continuous star formation in star-forming galaxies, whereas quiescent galaxies primarily grow via dry mergers (e.g., van der Wel et al. 2014; Whitaker et al. 2017). While high-redshift quiescent galaxies are compact at formation, often referred to as "red nuggets" (e.g., Damjanov et al. 2009), Fig. 8 indicates that they continue to grow in size down to $z \sim 0.5$, a trend that can be driven by minor mergers and other accretion processes (e.g., Newman et al. 2012; Belli et al. 2015). However, part of the observed size growth of quiescent galaxies may be attributed to progenitor bias – as new, larger galaxies continue to quench and enter the quiescent ... size of the population, making the size evolution appear more dramatic than if individual galaxies were tracked over time (e.g., Barro et al. 2013; Carollo et al. 2013).

The disk sizes of star-forming galaxies increase from ~1.4 kpc at $z \sim 5$ to 3.4 kpc by $z \sim 0.5$, consistent with expectations from inside-out growth models, where gas accretion and star formation preferentially occur in the outskirts (e.g., Patel et al. 2012; Morishita et al. 2014; Matharu et al. 2024). The disk sizes of quiescent galaxies remain small and are similar to, or smaller than, their bulges, at least out to $z \sim 2$, where the disk size increases to about 2.6 kpc. However, the scatter is significantly higher, making it difficult to draw meaningful conclusions about the disk sizes of quiescent galaxies. The bulge sizes for both star-forming and quiescent galaxies exhibit a mild evolution with redshift. Star-forming galaxies grow by about 0.6 kpc, reaching ∼1.2 kpc by $z \sim 0.5$. Quiescent galaxies are slightly more compact and, at high redshift, have bulges of about 0.4 kpc, increasing to about 1.2 kpc by $z \sim 0.6$. The persistence of small bulge sizes in both populations suggests that bulges reach their final configuration early, while the surrounding disks continue to evolve, particularly in star-forming galaxies. This is consistent with models in which early compaction events, such as mergers or disk instabilities, form a central bulge, after which the fate of the galaxy depends on the availability of fresh gas for continued star formation or quenching mechanisms (e.g., Barro et al. 2017; Tacchella et al. 2018).

4.3. Evolution of the stellar mass surface density for quiescent and star-forming galaxies

To investigate the relationship between the compactness of a galaxy and its star formation activity, we calculated the stellar mass surface density, Σ_e, which is the mass contained within the Sérsic effective radius, given by $\Sigma_e = M_\star/2\pi r_e^2$. Fig. 9 shows Σ_e as a function of stellar mass for quiescent and star-forming galaxies of $\log M_\star/\mathrm{M}_\odot > 9$, to facilitate comparison with the existing literature, in six redshift bins at $0.5 < z < 6$. This figure demonstrates that quiescent galaxies are more compact, with higher surface mass densities than those of star-forming galaxies, and that quiescent galaxies become increasingly dense at earlier times. This finding is in good agreement with previous work, e.g., Barro et al. (2017), which shows this relation out to $z \sim 3$. Our results indicate that this relation extends out to $z \sim 5$ and that quiescent galaxies increase in compactness the earlier they form. This is consistent with the observed compactness of some of the earliest quiescent galaxies found by JWST (Carnall et al. 2023; de Graaff et al. 2025; Weibel et al. 2024; Ito et al. 2024; Wright et al. 2024).

5. Conclusions

LA FIN

This work presents a catalog of galaxy morphologies measured from JWST imaging of the major extragalactic surveys CEERS, GO[illegible] JWST Archive. The catalog contains morphology information for more than 340 000 sources, detected on NIRCam LW stacks, with photometric [illegible] with two independent models of brightness profiles: a single Sérsic model a[illegible]OR++.

Nous n'avons qu'effleuré ce que ce catalogue de la forme de 340 000 galaxies peut nous apprendre sur l'évolution des galaxies et de l'Univers.

To validate our measurements, we compared our results with those from the literature obtained using independent methods and software, and we find good consistency. To demonstrate the scientific application, we used our morphological measurements i[illegible] the DJA EAZY catalogs. We investigated the relation between galaxy morphology, UVJ colors as an indicator of star formation activity and redshift. We summarize our results as follows:

Nous avons confirmé l'existence d'une très bonne corrélation entre la compacité d'une galaxie et le fait qu'elle produise ou non des étoiles. Nous avons également mesuré l'évolution de la taille de ces galaxies à travers les ères cosmiques, et surtout comment leur forme a varié.

– Using UVJ color selection, we find that early-type, bulge-[illegible]cent region, whereas late-type, disk-dominated galaxies exhibit blue, star-forming colors. We also observe a bimodality in these distributions, with some populations of quiescent galaxies that are disk-dominated, as well as star-forming galaxies [illegible];
– The two-component fits reveal that low B/T galaxies preferentially occupy the star-forming UVJ region, while high B/T galaxies populate the quiescent region. At $z > 3$, however, we observe a population of high B/T and bulge-dominated galaxies, consistent with a blue nugget phase;
– The Sérsic effective radius (r_e), disk effective radius ($r_{\rm disk}$), and bulge effective radius ($r_{\rm bulge}$) all show a decreasing trend with increasing redshift. Star-forming galaxies exhibit systematically larger sizes compared to quiescent galaxies at all redshifts, consistent with prior studies. Quiescent galaxies, while smaller than star-forming ones, show a steeper increase in their effective radius with time;
– Quiescent galaxies are significantly more compact than their star-forming counterparts, leading to high stellar mass surface densities (Σ_e). We find that Σ_e for quiescent galaxies is nearly an order of magnitude higher at $z \sim 4$ compared to $z \sim 1$, consistent with the observed compactness of some of the earliest quiescent galaxies observed by JWST.

This morphological catalog is a valuable addition to the DJA, enabling a range of in-depth studies of the morphological transformations associated with galaxy evolution.

Data availability

Our catalog is available at the CDS via anonymous ftp to cdsa[illegible]s:// cdsarc.cds.unistra.fr/viz-bin/cat/J/A+A/699/A343. It is al[illegible] code used to run the model fitting and the notebooks used to analyze the res[illegible] GitHub under the GNU GPL v3.0 license.

Notre catalogue est accessible à toustes les chercheureuses qui pourraient être intéressé.es !

Car c'est ce qu'il y a de bien dans le monde scientifique : les résultats sont généralement partagés pour faire progresser la connaissance collective de l'humanité !

Acknowledgements. The data products presented herein were retrieved from the [illegible] (DAWN), which is funded by the Danish National Research Foundation under grant [illegible]re-taria[illegible] for Education, Research and Innovation (SERI) under contract number MB22.00072. [illegible] Aurelien Genin at the Cosmic DAWN Center, under the supervision of Marko Shuntov. This internship h[illegible]le thanks to the financial support of the "Space: Science and Challenges of Space" chair at Ecole polytechnique, financed by ArianeGroup and Thales Alenia Space, as well as an Erasmus+ internship grant.

References

Allen, N., Oesch, P. A., Toft, S., et al. 2025, A&A, 698, A30
Barro, G., Faber, S. M., Pérez-González, P. G., et al. 2013, ApJ, 765, 104
Barro, G., Faber, S. M., Pérez-González, P. G., et al. 2014, ApJ, 791, 52
Barro, G., Faber, S. M., Koo, D. C., et al. 2017, ApJ, 840, 47
Belli, S., Newman, A. B., & Ellis, R. S. 2015, ApJ, 799, 206
Belli, S., Newman, A. B., & Ellis, R. S. 2019, ApJ, 874, 17
Berman, E. M., McCleary, J. E., Koekemoer, A. M., et al. 2024, AJ, 168, 174
Bertin, E. 2011, in Astronomical Data Analysis Software and Systems XX, eds. I. N. Evans, A. Accomazzi, D. J. Mink, & A. H. Rots, Astronomical Society of the Pacific Conference Series, 442, 435
Bertin, E., & Arnouts, S. 1996, A&AS, 117, 393
Bertin, E., Schefer, M., Apostolakos, N., et al. 2020, in Astronomical Data Analysis Software and Systems XXIX, eds. R. Pizzo, E. R. Deul, J. D. Mol, J. de Plaa, & H. Verkouter, Astronomical Society of the Pacific Conference Series, 527, 461
Brammer, G., van Dokkum, P. V., & Coppi, P. 2008, ApJ, 686, 1503
Carnall, A. C., McLure, R. J., Dunlop, J. S., et al. 2023, Nature, 619, 716
Carollo, C. M., Bschorr, T. J., Renzini, A., et al. 2013, ApJ, 773, 112
Conselice, C. J. 2003, ApJS, 147, 1
Conselice, C. J. 2014, ARA&A, 52, 291
Cortese, L., Catinella, B., & Smith, R. 2021, PASA, 38, e035
Daddi, E., Renzini, A., Pirzkal, N., et al. 2005, ApJ, 626, 680

Damjanov, I., McCarthy, P. J., Abraham, R. G., et al. 2009, ApJ, 695, 101
de Graaff, A., Setton, D. J., Brammer, G., et al. 2025, Nat. Astron., 9, 280
de Vaucouleurs, G. 1959, Handb. Phys., 53, 275
Dekel, A., & Burkert, A. 2014, MNRAS, 438, 1870
D'Eugenio, F., Pérez-González, P. G., Maiolino, R., et al. 2024, Nat. Astron., 8, 1443
Donnan, C. T., McLure, R. J., Dunlop, J. S., et al. 2024, MNRAS, 533, 3222
Eisenstein, D. J., Willott, C., Alberts, S., et al. 2023, arXiv e-prints, [arXiv:2306.02465]
Ester, M., Kriegel, H.-P., Sander, J., & Xu, X. 1996, in Second International Conference on Knowledge Discovery and Data Mining (KDD'96), Proceedings of a conference held August 2–4, 226
Fall, S. M., & Efstathiou, G. 1980, MNRAS, 193, 189
Finkelstein, S. L., Bagley, M. B., Ferguson, H. C., et al. 2023, ApJ, 946, L13
Fischler, M., & Bolles, R. 1981, Commun. ACM, 24, 381
Grogin, N. A., Kocevski, D. D., Faber, S. M., et al. 2011, ApJS, 197, 35
Gunn, J. E., & Gott, III, J. R. 1972, ApJ, 176, 1
Heintz, K. E., Brammer, G. B., Watson, D., et al. 2025, A&A, 693, A[illegible]
Hubble, E. P. 1936, Realm of the Nebulae (New Haven: Yale University Press)
Ito, K., Valentino, F., Brammer, G., et al. 2024, ApJ, [illegible]4, 192
Kawinwanichakij, L., Silverman, J. D., Ding, X., et al. 2021, [illegible] 38
Koekemoer, A. M., Aussel, H., [illegible] D., et al. 2007, ApJS, 172, 196
Koekemoer, A. M., Faber, S. M., Ferguson, H. C., et al. 2011, ApJS, 197, 36
Kümmel, M., Bertin, E., Schefer, M., et al. 2020, in Astronomical Data Analysis Software and Systems XXIX, eds. R. Pizzo, E. R. Deul, J. D. Mol, J. de Plaa, & H. Verkouter, Astronomical Society of the Pacific Conference Series, 527, 29
Larson, R. B., Tinsley, B. M., & Caldwell, C. N. 1980, ApJ, 237, 692
Leauthaud, A., Massey, R., Kneib, J.-P., et al. 2007, ApJS, 172, 219
Lintott, C. J., Schawinski, K., Slosar, A., et al. 2008, MNRAS, 389, 1179
Lotz, J. M., Primack, J., & Madau, P. 2004, AJ, 128, 163
Matharu, J., Nelson, E. J., Brammer, G., et al. 2024, A&A, 690, A64
Mo, H. J., Mao, S., & White, S. D. M. 1998, MNRAS, 295, 319
Moore, B., Katz, N., Lake, G., Dressler, A., & Oemler, A. 1996, Nature, 379, 613
Moore, B., Lake, G., & Katz, N. 1998, ApJ, 495, 139
Moran, S. M., Ellis, R. S., Treu, T., et al. 2007, ApJ, 671, 1503
Morishita, T., Ichikawa, T., & Kajisawa, M. 2014, ApJ, 785, 18
Moutard, T., Sawicki, M., Arnouts, S., et al. 2018, MNRAS, 479, 2147
Newman, A. B., Ellis, R. S., Bundy, K., & Treu, T. 2012, ApJ, 746, 162
Oke, J. B. 1974, ApJS, 27, 21
Omand, C. M. B., Balogh, M. L., & Poggianti, B. M. 2014, MNRAS, 440, 843
Ormerod, K., Conselice, C. J., Adams, N. J., et al. 2024, MNRAS, 527, 6110
Patel, S. G., Holden, B. P., Kelson, D. D., et al. 2012, ApJ, 748, L27
Peng, Y., Lilly, S. J., Kovac, K., et al. 2010, ApJ, 721, 193
Planck Collaboration VI. 2020, A&A, 641, A6
Quilley, L., & de Lapparent, V. 2022, A&A, 666, A170
Rieke, M., Kelly, D., & Horner, S. 2005, in SPIE Optics + Photonics, 5904
Rix, H.-W., Barden, M., Beckwith, S. V. W., et al. 2004, ApJS, 152, 163
Robitaille, T. 2018, https://doi.org/10.5281/zenodo.1162674
Schawinski, K., Urry, C. M., Simmons, B. D., et al. 2014, MNRAS, 440, 889
Schreiber, C., Elbaz, D., Pannella, M., et al. 2016, A&A, 589, A35
Sérsic, J. L. 1963, Bol. Asoc. Argentina Astron. La Plata Argentina, 6, 41
Shen, S., Mo, H. J., White, S. D. M., et al. 2003, MNRAS, 343, 978
Shibuya, T., Ouchi, M., & Harikane, Y. 2015, ApJS, 219, 15
Somerville, R. S., Behroozi, P., Pandya, V., et al. 2018, MNRAS, 473, 2714
Tacchella, S., Carollo, C. M., Renzini, A., et al. 2015, Science, 348, 314
Tacchella, S., Dekel, A., Carollo, C. M., et al. 2016, MNRAS, 458, 242
Tacchella, S., Carollo, C. M., Förster Schreiber, N. M., et al. 2018, ApJ, 859, 56
Toft, S., Zabl, J., Richard, J., et al. 2017, Nature, 546, 510
Trujillo, I., Conselice, C. J., Bundy, K., et al. 2007, MNRAS, 382, 109
Valentino, F., Brammer, G., Gould, K. M. L., et al. 2023, ApJ, 947, 20
van der Wel, A., Bell, E. F., Häussler, B., et al. 2012, ApJS, 203, 24
van der Wel, A., Franx, M., van Dokkum, P. G., et al. 2014, ApJ, 788, 28
van Dokkum, P. G., Nelson, E. J., Franx, M., et al. 2015, ApJ, 813, 23
Varadaraj, R. G., Bowler, R. A. A., Jarvis, M. J., et al. 2024, MNRAS, 533, 3724
Weibel, A., Oesch, P. A., Barrufet, L., et al. 2024, MNRAS, 533, 1808
Whitaker, K. E., Bezanson, R., van Dokkum, P. G., et al. 2017, ApJ, 838, 19
Williams, R. J., Quadri, R. F., Franx, M., van Dokkum, P., & Labbé, I. 2009, ApJ, 691, 1879
Wright, L., Whitaker, K. E., Weaver, J. R., et al. 2024, ApJ, 964, L10
Yang, L., Kartaltepe, J. S., Franco, M., et al. 2025, COSMOS-Web: Unraveling the Evolution of Galaxy Size and Related Properties at $2 < z < 10$
York, D. G., Adelman, J., Anderson, John E., J., et al. 2000, AJ, 120, 1579
Zolotov, A., Dekel, A., Mandelker, N., et al. 2015, MNRAS, 450, 2327

Et puisque nous avons cité le travail d'un grand nombre de personnes différentes, nous devons les citer correctement.

Merci d'avoir lu mon papier, et félicitations pour avoir atteint la fin ! J'espère que vous avez appris de nouvelles choses sur la vie des galaxies, et que ma tentative de rendre ce document compréhensible a été suffisamment claire.

Aurélien Genin
https://astroaure.github.io

J'ai eu l'idée de faire cette version simplifiée de mon papier grâce à Claire Lamman qui fait un travail formidable ! Allez voir clairelamman.com pour plus de projets similaires. Et comme elle, j'ai utilisé la police XKCD : https://github.com/ipython/xkcd-font
Le dessin du JWST au début vient du MAST.